RSC Advances

ROYAL SOCIETY OF CHEMISTRY

www.rsc.org/advances

Table of contents

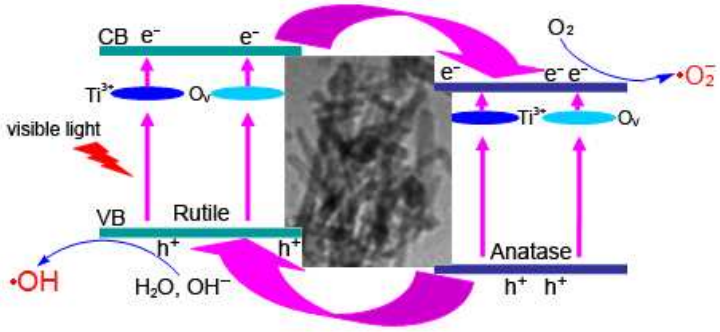

Ti^{3+} self-doped TiO_2(A)/TiO_2(R) heterojunctions were synthesized and the samples exhibit higher visible light photocatalytic activity.

Fabrication of Ti^{3+} self-doped TiO_2(A) nanoparticle/TiO_2(R) nanorod heterojunctions with enhanced visible-light-driven photocatalytic properties

Rongrong Fu [a], Shanmin Gao [a,b,*], Hui Xu [a], Qingyao Wang [a], Zeyan Wang [b], Baibiao Huang[b,*], Ying Dai[b]

[a] College of Chemistry and Materials Science, Ludong University, Yantai, 264025, China.

[b] State Key Laboratory of Crystal Materials, Shandong University, Jinan 250100, China.

Abstract

Ti^{3+} self-doped TiO_2(A)/TiO_2(R) heterojunctions comprising anatase TiO_2 (TiO_2(A)) nanoparticles and rutile TiO_2 (TiO_2(R)) nanorods were synthesized by a simple hydrothermal method using Zn as the reductant. The structure, crystallinity, morphology, and chemical state of the as-prepared samples were characterized by X-ray diffraction, transmission electron microscopy, high-resolution transmission electron microscopy, X-ray photoelectron spectroscopy, and UV–Vis diffuse reflectance spectroscopy. The heterojunction architectures and Ti^{3+} contents could be controlled by adjusting the temperature of the hydrothermal treatment. Zn acts as a reducing agent and Zn^{2+} stabilizes the oxygen vacancies. Meanwhile, the generated ZnO clusters promote phase transformation from TiO_2(A) to TiO_2(R). The visible-light photocatalytic degradation of dyes was analyzed. The Ti^{3+} self-doped TiO_2(A)/TiO_2(R) heterojunctions exhibited an extended visible light absorption and higher visible-light photocatalytic activity than that of commercial P25 TiO_2 in the photodegradation of Methylene blue and Rhodamine B under visible-light irradiation ($\lambda \geq 400$ nm). Ti^{3+} self-doping expanded the light-response range, and the formed heterojunctions at the interface of TiO_2(A)

nanoparticles and TiO_2(R) nanorods efficiently reduced the recombination of photoinduced electron–hole pairs. This self-doping increased the lifetime of charge carriers by 15 times that of P25 TiO_2 and enhanced the corresponding photocatalytic activity of the self-doped heterojunctions.

Key words: Ti^{3+} self-doped, TiO_2(A)/TiO_2(R), heterojunctions, visible-light photocatalytic

1. Introduction

TiO_2 is an active photocatalyst used in solar energy conversion, decontamination of polluted water, and water-splitting.[1] However, TiO_2 can only absorb a small portion of solar spectra in the UV region because of its wide gap energy (anatase TiO_2 (TiO_2(A)), 3.2 eV; rutile TiO_2 (TiO_2(R)), 3.0 eV) and the high recombination rate of photo-induced electron–hole pairs on or near its surface.[2] Metal cation doping, nonmetal anion doping, semiconductor heterojunctions, and surface modification with noble metal have been performed to alter the electronic structures and physical properties of TiO_2.[3] However, the traditional incorporation of impurities causes thermal instability and trapping of photoinduced electrons by the doped ions; this incorporation reduces the photocatalytic efficiency.[4] Given these processes, ion-doped TiO_2 photocatalysts with high visible-light activity should be developed to meet the requirements for practical applications.

Reduced TiO_2 (TiO_{2-x}) containing Ti^{3+} or oxygen vacancies (O_V) increases the visible-light response of TiO_2.[5] Local states can be formed at the bottom of the conduction band (CB) by introducing Ti^{3+} or O_V in TiO_2; hence, TiO_2(A) and TiO_2(R) have visible-light absorption performance.[6] Ti^{3+} are defects that function as electron capture agents, increase the electrical conductivity, and accelerate the transfer of electrons and holes.[7] The separation efficiencies of

electrons and holes can be controlled by adjusting the concentration of Ti^{3+} or O_V.[8] Previous theoretical calculations indicated that the Ti^{3+} concentration should be high enough to induce a continuous vacancy band of electronic states just below the CB edge of TiO_2 and efficiently achieve visible-light activities.[9] By contrast, low Ti^{3+} doping concentrations produce localized O_V states that deteriorate electron mobility and exhibit negligible visible photoactivities.[10]

The morphology of TiO_2 crystals primarily determines the photocatalytic performance.[11] One-dimensional (1D) structures beneficially increase the transfer rate of interfacial carriers because of the increase in delocalized carriers from their free movements throughout the crystal.[12] In addition, the separation of 1D photocatalysts from the solution is easier than that of spherical particles. A and R are major crystalline phases of TiO_2 that are commonly used in photocatalytic reactions.[13] TiO_2(R) is preferential for growth in [001] direction, which elongates the nanorods. In addition, TiO_2(R) is less photoactive than TiO_2(A). However, the dispersion of relatively small crystals of A on large TiO_2(R) nanorods and TiO_2(A)/TiO_2(R) heterojunctions yields A–R synergistic effects. These effects facilitate the transfer of photogenerated electrons from the CB of the TiO_2(R) nanorods to TiO_2(A), thereby improving the charge separation efficiency and enhancing the photocatalytic activity.[14] The coupling of TiO_2(A) nanoparticles with TiO_2(R) nanorods forms a 0D/1D heterogeneous nanostructures, which exhibit structures and special properties that are distinct from those of conventional spherical A/R composites.[15] In addition, hydrothermal treatments have elicited attention in the preparation of TiO_2 nanocrystals with various morphologies because they directly produce various well-crystallized nanocrystallites at short period reaction times.[16]

In this article, we fabricated a series of Ti^{3+} self-doped TiO_2(A)/TiO_2(R) heterojunctions by a

simple and surfactant-free hydrothermal method at different temperatures; these samples comprised TiO_2(A) nanoparticles and TiO_2(R) nanorods. Their photocatalytic performance towards the visible-light degradation of methylene blue (MB) and rhodamine B (RhB) were examined. The results indicated that Ti^{3+} self-doping enhanced the photoabsorption capability of TiO_2 in the visible region. The heterojunctions formed between TiO_2(A) nanoparticles and TiO_2(R) nanorods improved the separation efficiency of the charge carriers, thereby improving the photocatalytic activities for MB and RhB degradation. The formation and photocatalytic mechanisms of Ti^{3+} self-doped TiO_2(A)/TiO_2(R) heterojunctions were determined.

2. Materials and Methods

2.1 Materials

$Ti(SO_4)_2$, Zn powder, and NaOH were reagent-grade and obtained from Ruijinte Chemical Reagent Co. (Tianjin, China) without further purification. Double distilled water was used throughout the experiments.

2.2 Sample preparation

In a typical procedure, 1.52 g of $Ti(SO_4)_2$ powder was dissolved in 20 mL deionized water. Subsequently, 0.1 g Zn powder was added to the $Ti(SO_4)_2$ solution under vigorous stirring. The suspension was continuously stirred for 30 min at room temperature. The mixture solution was then filtered to yield a clear and bluish violet solution. Following the filtration, 0.6 mol/L NaOH was introduced to the resultant solution to adjust the pH to 4–5 and form a bluish violet precipitate. The reaction mixture was transferred into a Teflon-lined stainless steel autoclave with a capacity of

50 mL and maintained at different temperatures ranging from 140 °C to 180 °C for 24 h in an electric oven. After the mixture was cooled to room temperature, blue or light-blue precipitates were collected and washed thrice with deionized water and absolute ethanol to remove any residual impurities. The precipitates were then oven dried at 80 °C for 3 h.

2.3 Characterization

The phases of the final products were identified using an X-ray diffractometer (XRD; Rigaku D/max-2500VPC) with Ni-filtered Cu-Kα radiation from 20° to 80° at a scanning rate of 0.02° s^{-1}. Transmission electron microscopy (TEM) and high-resolution TEM (HRTEM) measurements were carried out on a JEOL-2100 microscope. X-ray photoelectron spectra (XPS) measurements were performed on an X-ray photoelectron spectrometer (VG Micro Tech ESCA 3000) using monochromatic Al-Kα with a photon energy of 1486.6 eV and a reference C1s peak of 284.6 eV. UV–Vis diffuse reflection spectra (DRS) were recorded on a Shimadzu UV-2550 UV-Vis spectrophotometer at room temperature from 200 nm to 800 nm.

2.4 Photocatalytic Activity Measurements

The photocatalytic performances of the as-prepared TiO_2(A)/TiO_2(R) heterojunctions were evaluated by the degradation of MB and RhB dyes. A Xe lamp (power, 300 W; PLS-SXE300, Beijing Trusttech Co., Ltd., China) equipped with a UV cutoff filter was used as a light source to provide visible light ($\lambda \geq 400$ nm). During the degradation of MB and RhB dyes, a total sample mass of 0.04 g was added to 100 mL MB or RhB aqueous solution (concentration, 5.0×10^{-4} M) in a customized quartz reactor. The concentration of MB and RhB was monitored by UV–Vis spectroscopy. Each suspension was magnetically stirred in the dark for 30 min to obtain a good

dispersion and reach an adsorption–desorption equilibrium between MB or RhB and the photocatalysts; the suspensions were then irradiated by visible light. After 10 min intervals during visible-light illumination, about 3 mL aliquots were taken out and centrifuged to remove the trace particles. The absorbance of the centrifuged solution was measured from 200 nm to 800 nm using a UV–Vis spectrophotometer (Shimadzu UV-2550). During the photoreactions, no oxygen was bubbled into the suspension. Similar measurements were also performed on the pure P25 TiO_2 for comparative purposes.

To detect the active species during photocatalytic reactivity, active hydroxyl radicals (•OH) were obtained by visible-light irradiation. The experimental procedure was similar as that of photocatalysis, except that the aqueous solution of MB or RhB was replaced by a 5×10^{-4} M terephthalic acid (TA) solution with 2×10^{-3} M NaOH. Following the irradiation for 10 min, 2.0 mL solution was taken out and centrifuged for fluorescence spectroscopy by using a Perkin Elmer LS 55 fluorescence spectrometer. An excitation light wavelength of 320 nm was used to record the fluorescence spectra. No oxygen was bubbled into suspension during the photoreactions.[17]

3. Results and Discussion

3.1 Characterization of TiO_2(A)/TiO_2(R) heterojunctions

The crystalline structure of TiO_2(A)/TiO_2(R) heteojunctions during hydrothermal treatments was determined by XRD. The A-to-R ratio was estimated as follows:[18]

$$W_R = 1.26I_R / (I_A + 1.26I_R) \qquad (1.1)$$

$$W_A = 1 - W_R \qquad (1.2)$$

where W_A and W_R are the fractions of TiO_2(A) and TiO_2(R) in the heterojunction samples, I_A is the X-ray integrated intensities of the (101) diffraction of A. Because of the abnormal growth of R, the intensity of rutile (101) was taken as I_R.[19]

The average crystallite sizes of the samples were estimated from the TiO_2(A) peak (101) and TiO_2(R) peak (101) by using the Debye–Sherrer formula given by Eq. (1.3):

$$d = K\lambda/(\beta\cos\theta) \qquad (1.3)$$

where d is the particle size, λ is the wavelength of the X-ray radiation (0.15406 nm), K is the shape coefficient, θ is the diffraction angle, and β is the full width at half maximum (FWHM) of the selected diffraction peak.

The XRD patterns (Fig. 1) revealed that all the products were mixtures of TiO_2(A) and TiO_2(R). The hydrothermal temperature markedly influenced the phase transformation and composition of the crystalline structure of TiO_2. XRD analysis indicated that the products were mixtures of poorly crystallized and amorphous TiO_2 at a hydrothermal temperature are 140 °C. The peaks at 2θ = 25.2°, 37.8°, 48.0°, 53.9°, 62.7°, and 75.0° were indexed to (101), (004), (200), (105), (204), and (215) crystal planes of TiO_2(A) (JCPDF No. 21-1272), respectively. The XRD patterns exhibited weak diffraction lines at 2θ = 27.4°, 36°, 41.1°, and 54.1°, which implied the presence of TiO_2(R) (JCPDS Card No. 21-1276). The A-to-R ratio in the sample at 140 °C for 24 h was estimated to be 89:11. TiO_2(R) was the main product for hydrothermal treatment temperatures reaching 180 °C. The peaks at 2θ = 27.4°, 35.9°, 41.1°, 43.9°, 54.3°, 56.4°, 62.8°, and 69.0° were respectively assigned to (110), (101), (200), (111), (210), (211), (220), (002), and (301) planes of TiO_2(R). The R content increased from 33.5 and 47.9 to 88.6 wt% when the hydrothermal treatment temperatures correspondingly

increased from 150 °C and 160 °C to 180 °C, respectively. These results indicated that the ratio of the diffraction peak intensities of A(101) and R(101) gradually increased with the treatment temperature, suggesting the transformation of A into R phase with the treatment temperature. In addition, the average crystallite sizes of the heterojunction samples prepared at various treatment temperatures was calculated from the FWHM of the diffraction peak via the Debye–Scherrer equation. Table 1 reveals that the high treatment temperature causes the crystallite growth in TiO_2(A) and TiO_2(R).

Table 1. The average crystal size and ratio of A(101)/R(101) of the TiO_2(A)/TiO_2(R) heterojunctions.[a]

Hydrothermal temperature (°C)	140	150	160	180
Crystalline size of A (nm)	4.3	6.1	7.8	15.2
Crystalline size of R (nm)	2.3	4.5	18.8	26.3
Ratio of A(101)/R(101)	89:11	66.5:33.5	52.1:47.9	11.4:88.6

[a] The crystal size was determined from the XRD peak (101) and Debye–Scherer equation.

The XRD patterns suggested that the R(101) peak and half-peak breadth were stronger and narrower than those of (110) the reflection in standard TiO_2(R), which indicated that the R structure is growth-oriented. This result was proved by the morphology and microstructure of the TiO_2(A)/TiO_2(R) heterojunction samples in TEM and HRTEM images.

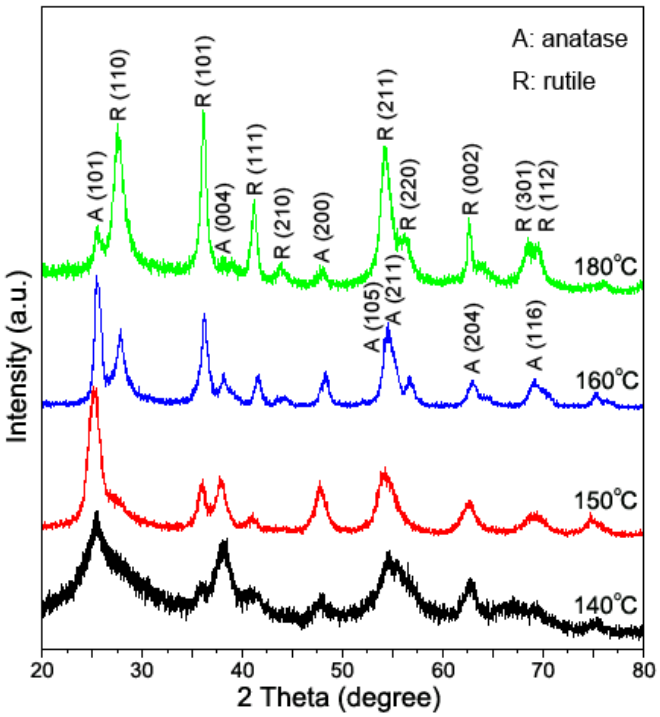

Fig. 1. XRD patterns of TiO_2(A)/TiO_2(R) heterojunction samples obtained at different hydrothermal temperatures.

Fig. 2 shows the TEM and HRTEM images of the heterojunction samples obtained at different hydrothermal treatment temperatures. The products were formed as large aggregates at 140 °C (Fig. 2A), which comprised several small particles. The morphology of the products grew regularly and comprised abundant nanoparticles and some nanorods with increasing temperature (Fig. 2B). TEM results at 160 °C showed that the heterojunction samples exhibited good crystallization, most of which were nanorods (Fig. 2C). The corresponding HRTEM (Fig. 2D) implied that the heterojunctions were formed. These nanoparticles exhibited a lattice spacing *d* of 0.35 nm for the (101) plane of TiO_2(A). The distance between the lattice fringes of 0.33 nm in the nanorods was ascribed to the interplanar distance of the (110) plane of TiO_2(R), which was consistent with the XRD results. The nanoparticles and nanorods were in the polycrystalline A and single crystalline R

phases, respectively; both materials formed the TiO_2(A)/TiO_2(R) heterojunction. For treatment temperatures reaching 180 °C, the products comprised nanorods with some nanoparticles attached on their surfaces (Fig. 2E). The interplanar spacing of a pure nanorod (Fig. 2F) was around 0.32 nm, which was in agreement with the value of *d* of the (110) planes of TiO_2(R). TiO_2(R) nanorods were preferably grown in the [001] direction,[20] which was consistent with the XRD data.

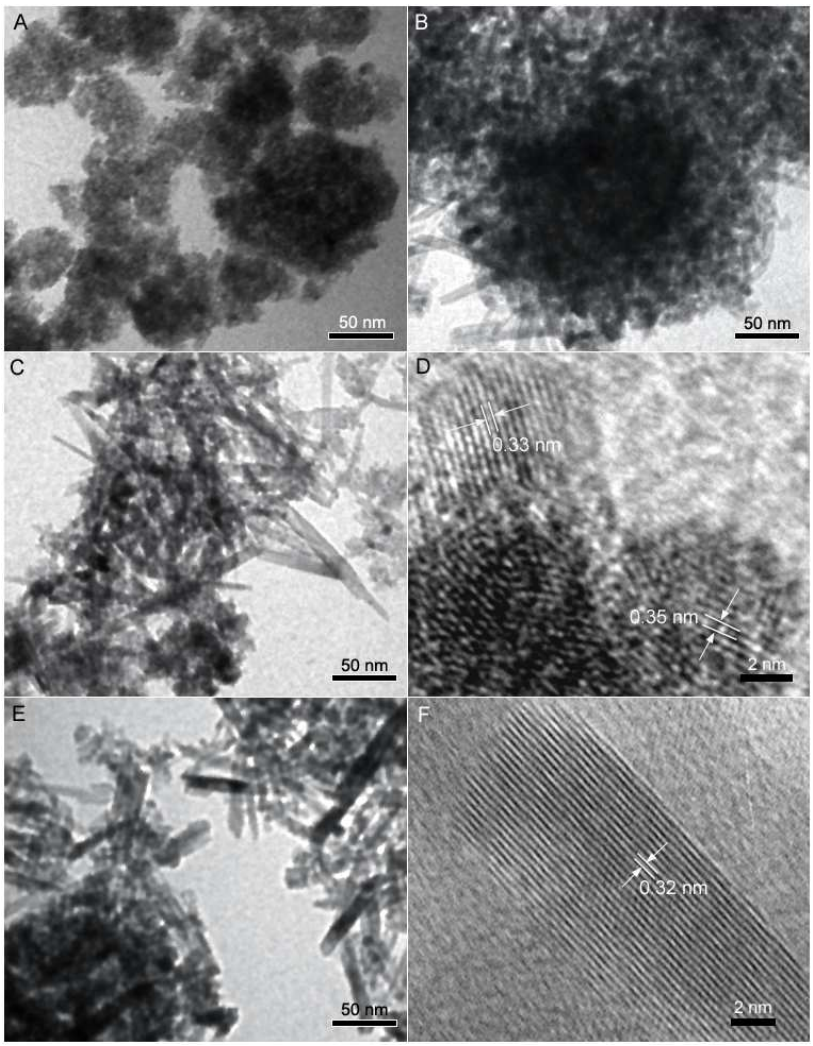

Fig. 2. TEM and HRTEM images of the samples obtained at 24 h for hydrothermal treatment temperatures of (A): 140 °C, (B): 150 °C, (C and D): 160 °C, (E and F): 180 °C.

The chemical state and surface composition of Ti^{3+} self-doped TiO_2(A)/TiO_2(R) heterojunctions

were studied by XPS. Fig. 3 illustrates the high-resolution XPS spectra of Ti 2p, O 1s, and Zn 2p, as well as the fitting results of the experimental data for Ti 2p and O 1s at 160 °C for 24 h.

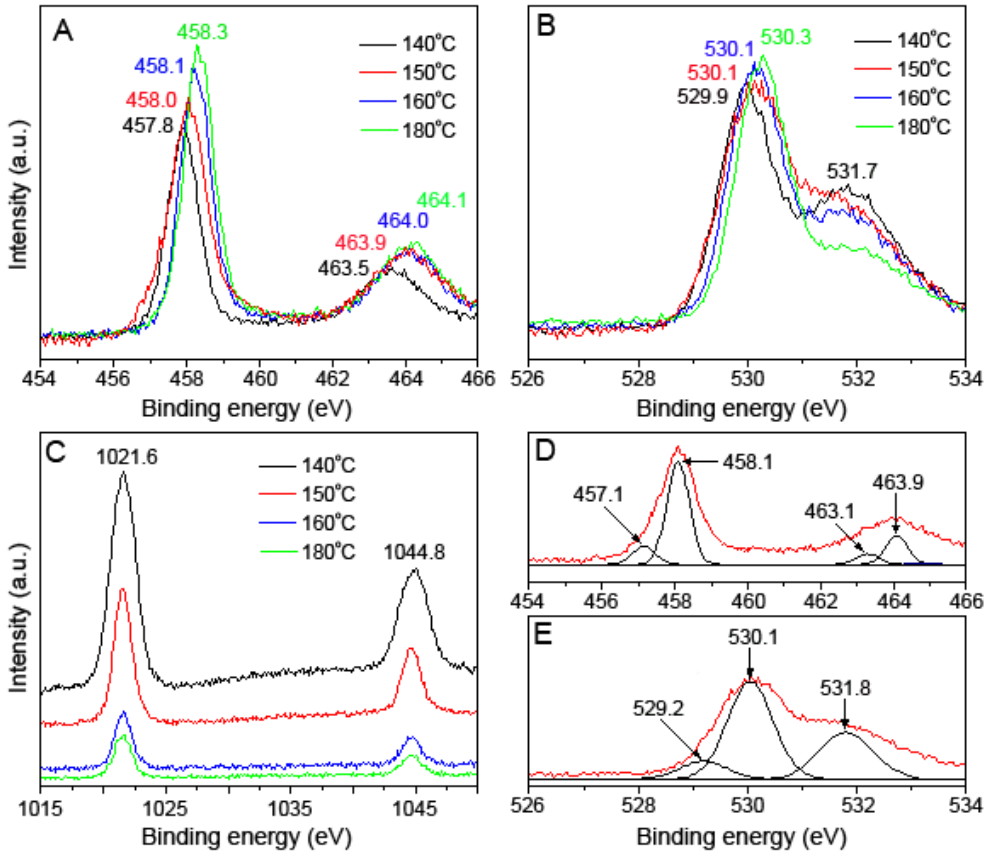

Fig. 3. High-resolution XPS spectra of (A) Ti 2p, (B) O 1s, and (C) Zn 2p; fitting results of the experimental data for (D) Ti 2p and (E) O 1s at 160 °C for 24 h.

Pure TiO_2 exhibited a typical binding energy at 459.4 and 464.7 eV that corresponded to the binding energies of Ti $2p_{3/2}$ and Ti $2p_{1/2}$.[21] Fig. 3A reveals that the Ti 2p3/2 and Ti 2p1/2 bands of the samples prepared at 160 °C were observed at 458.1 and ca. 464 eV, respectively; the latter was shifted by 1.3 eV with reference to pure TiO_2 particles. The fitting for the Ti $2p_{3/2}$ peak revealed the presence of a major peak at 458.1 eV with a shoulder at 457.1 eV. The Ti $2p_{1/2}$ peak was deconvoluted into two binding energies at 463.9 and 463.1 eV. The peaks at 458.1 and 463.9 eV were assigned to the $2p_{3/2}$ and $2p_{1/2}$ core levels of Ti^{4+}, respectively. Meanwhile, those at 457.1 and

463.1 eV were ascribed to the $2p_{3/2}$ and $2p_{1/2}$ core levels of Ti^{3+}, respectively (Fig. 3D). Binding energies were shifted to lower counterparts by 1.6, 1.4, and 1.1 eV for the TiO_2(A)/TiO_2(R) heterojunctions respectively obtained at 140 °C, 150 °C, and 180 °C. The shifts were attributed to the existence of Ov around Ti^{4+}; Ti^{3+} species were formed in the heterojunction samples to satisfy the requirement of charge equilibrium.[22] The shifts of the Ti 2p peak to low energies decreased with increasing treatment temperature, which indicated that the Ti^{3+} concentration decreased with the latter. Ti^{3+} is essentially a defective state and acts as a hole trap to promote charge separation and suppress the recombination of electron–hole pairs.[23]

The high-resolution O 1s spectra (Fig. 3B) comprised primary and secondary peaks with binding energies of about 530.0 and 531.7 eV, respectively. The primary and secondary peaks were respectively attributed to the lattice oxygen in TiO_2 and ZnO (i.e., Ti−O and Zn−O) and oxygen in surface hydroxyl groups for TiO_2 and ZnO (i.e., Ti−OH and Zn−OH).[24] The peak separation of the O 1s spectrum for the sample obtained at 160 °C exhibited three types of oxygen bands with binding energies of 529.2, 530.1, and 531.8 eV, respectively (Fig. 3E). The band at 529.2 eV was equivalent to surface defects like O_V with matrix of TiO_2. The peak intensity was connected to the variations in the concentration of O_V, which functioned as hole traps to promote charge transfer, induce catalytic activity, and inhibit the recombination of electron–hole pairs.[23] The band at 530.1 eV was attributed to the Ti(IV)–O or Zn–O bonds, while the peaks at 531.8 eV belonged to the surface oxygen that mainly consisted of the oxygen species of hydroxyl groups.[25] The abundant adsorbed water and hydroxyl groups on the surface could potentially trap the holes to form oxidative •OH and photodegrade organic molecules.[26] The peak intensity at ~531.7 eV continuously decreased with

increasing treatment temperature, indicating the decreased photocatalytic activity caused by the loss of hydroxyls.

Fig. 3C shows the high-resolution spectrum of Zn 2p. The peaks at 1021.6 and 1044.8 eV were ascribed to Zn $2p_{3/2}$ and Zn $2p_{1/2}$, respectively. The peak separation between Zn $2p_{3/2}$ and Zn $2p_{1/2}$ was 23.2 eV, which was assigned to the +2 oxidation state of Zn.[27]

The XRD patterns (Fig. 1) failed to exhibit any Zn oxides. In addition, Ti^{4+} was hardly replaceable with Zn^{2+} because of the large difference between the ionic radii of Zn^{2+} (0.88 Å) and Ti^{4+} (0.745 Å). Therefore, Zn could primarily exist in the form of ZnO clusters or be amorphous on the TiO_2 surface; this element could either be solute in the TiO_2 lattice or inlay in TiO_2 particles.[28] Zn^{2+} could weaken surface oxygen bonds, thereby increasing the probability of oxygen loss from the surface; the remaining electrons could be trapped at Ti^{4+} interstitials to form Ti^{3+}.[29] The peak intensity significantly decreased with increasing treatment temperature, which implied the reduction of Zn^{2+} concentration in the heterojunction samples.

3.2 Formation mechanism of Ti^{3+} self-doped TiO_2(A)/TiO_2(R) heterojunctions

Given the phase transformation from TiO_2(A) nanoparticles to TiO_2(R) nanorods with increasing treatment temperature, the recrystallization mechanism was tentatively proposed for the formation of Ti^{3+} self-doped TiO_2(A)/TiO_2(R) heterojunctions (Fig. 4).

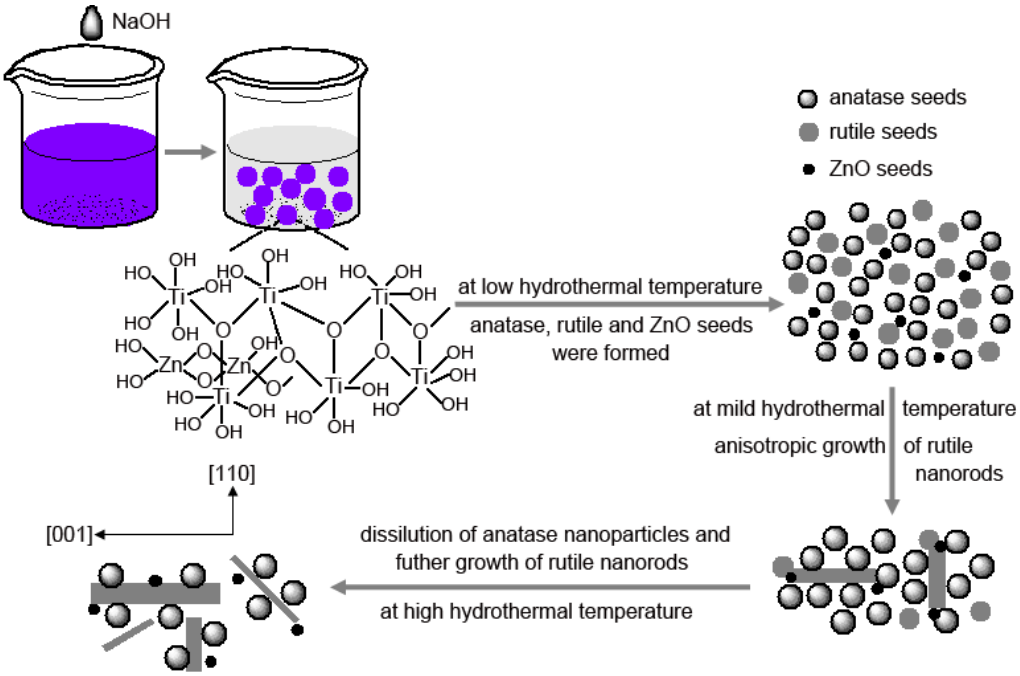

Fig. 4. Formation mechanism of TiO_2(A)/TiO_2(R) heterojunctions.

Precipitation reactions of Ti^{3+} and Zn^{2+} occurred between the OH^- and Ti^{4+} and Ti^{3+} and Zn^{2+}, respectively. At low treatment temperatures, the condensation–dehydration reaction occurred between the Ti^{4+}, Ti^{3+}, and Zn^{2+} with the –OH ligands to form Ti–O–Ti and Zn–O–Zn oxo species; competitions arose with the formation of A, R, and ZnO seeds. The anisotropic growth of TiO_2(R) nanorods was established at moderate and high treatment temperatures because R was at the thermodynamically stable phase; this process was accompanied by the consumption of small TiO_2(A) nanoparticles.[30]

During the growth of TiO_2 crystals, ZnO clusters functioned as chemical catalysts to reduce the activation energy and form R.[31] Zn^{2+} could affect the structure of O–Ti–O bonds and favor the formation of TiO_2(R) nanorods from amorphous titania and TiO_2(A).[32] Given the dependence of the growth rate of the crystal faces on the quantities of corners and edges of available coordination polyhedra, the growth of TiO_2(R) nanorods followed the sequence (110) < (100) < (101) < (001).[33]

XRD analysis revealed that TiO_2(R) nanorods grew along the [001] direction. The R structure developed into the main phase and the nanorods became the dominant components, suggesting that the particles were A and the nanorods were R. These results were substantiated by the HRTEM images (Figs. 2D and 2F).

3.3 Optical properties and photocatalytic activity

Fig. 5 show the UV–Vis spectra of the TiO_2(A)/TiO_2(R) heterojunction samples prepared at different hydrothermal treatment temperatures. In contrast to P25 TiO_2, all samples exhibited strong and broad absorption bands between 400 and 700 nm that covered the entire visible range. The enhanced visible-light absorption was attributed to the formation of Ti^{3+} species, which introduced a localized state in the forbidden band gap of TiO_2 approximately 0.75–1.18 eV below the CB edge of TiO_2.[34] The heterojunction samples obtained at 150 °C and 160 °C exhibited maximum absorption bands in the visible region. However, the visible-light absorption decreased for sufficiently high hydrothermal temperatures (180 °C) because of the reduction of Ti^{3+} and Ov. Thus, temperature markedly influenced the Ti^{3+} doping concentration by changing the electronic structure of TiO_2. Ti^{3+} self-doped TiO_2(A)/TiO_2(R) heterojunctions could be potential photocatalysts for solar energy-related applications because of their enhanced ability to absorb visible light.

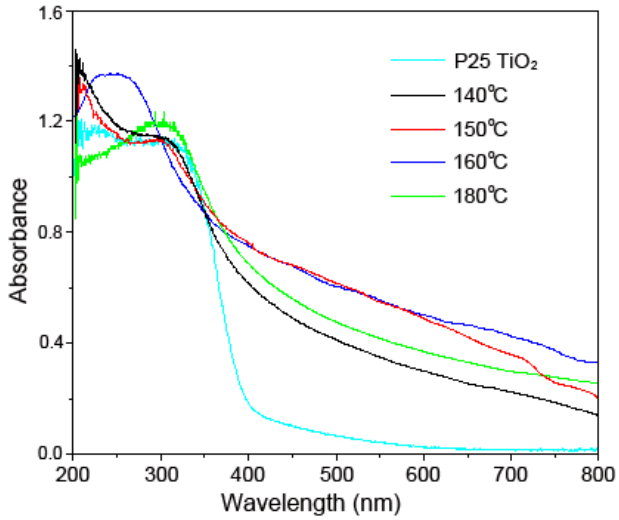

Fig. 5. UV–Vis spectra of TiO_2(A)/TiO_2(R) heterojunctions and P25 TiO_2.

Comparison of the adsorption and photodegradation abilities on MB and RhB solutions between TiO_2 heterojunction samples and P25 TiO_2 revealed that the former exhibited specific adsorption capacities (Figs. 6A and 6B). The heterojunctions obtained at 140 °C yielded the optimal adsorption capacity, in which nearly 25% of the dye molecules were adsorbed within 30 min. The rapid adsorption was attributed to the large surface area of the heterojunction samples. The adsorption capacity decreased with further increasing treatment temperature because of the reduced surface area.

The heterojunction samples displayed excellent visible-light photocatalytic activities (Figs. 6A and 6B). A comparative experiment with P25 was also performed; less than 5% of the degradation rate could be neglected. The samples prepared at 160 °C yielded the highest photocatalytic activity. About 99% of MB was decomposed by the heterojunction samples prepared at 160 °C after 60 min of visible-light irradiation. By contrast, 77%, 94%, and 85% of MB were decomposed by those prepared at 140 °C, 150 °C, and 180 °C under a fixed illumination time, respectively. Similar results on RhB decomposition were obtained under visible-light irradiation for

80 min. The results indicated that the heterojunction samples obtained at 160 °C obtained the best photocatalytic activity to decompose MB and RhB.

We measured the dynamic UV–Vis absorption spectra of MB and RhB solutions in the presence of the heterojunctions obtained at 160 °C for 24 h (Figs. 6C and 6D). The intensities of the characteristic absorption peaks of MB (~664 nm) and RhB (~554 nm) rapidly diminished with increased duration of visible-light irradiation. The peaks at 664 and 554 nm for MB and RhB were observed after 60 and 80 min of visible-light radiation. The corresponding changes in color of MB and RhB solutions with the increasing reaction time were shown in the insets in Figs. 6C and 6D.

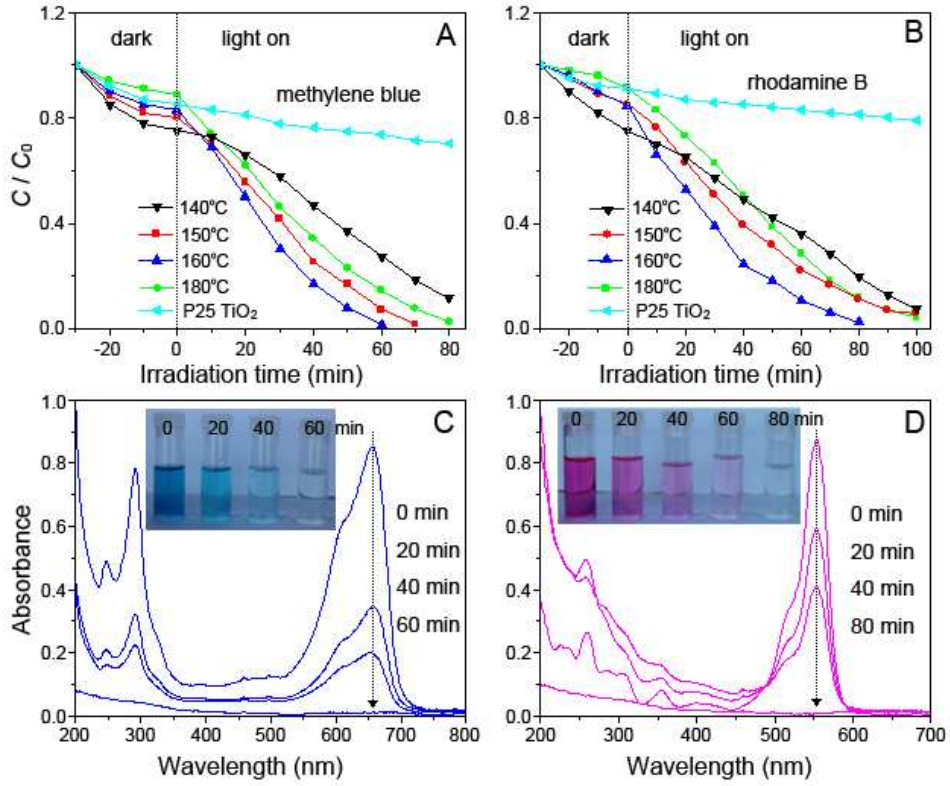

Fig. 6. (A and B): The adsorption and photodegradation of MB and RhB solutions by using P25 TiO_2, and the as-prepared heterojunction samples as photocatalysts under visible-light irradiation. (C and D): UV–Vis absorption spectra of MB and RhB solutions recorded at different times using the heterojunction samples obtained at 160 °C for 24 h as photocatalysts.

•OH exhibited a high oxidizing potential to degrade of MB and RhB during photocatalysis,[35] which was consistent with the fluorescence intensities tested by terephthalic acid photoluminescence (TA–PL) probing technique.[36] Fig. 7A shows the photoluminescence (PL) emission spectra excited at 320 nm from the TA solution, which were measured every 10 min of illumination. The PL intensity and number of •OH at about 425 nm gradually increased with the irradiation time. The maximum number of •OH radicals was formed by using the heterojunction samples obtained at 160 °C for 24 h during the photoreaction, which was in agreement with the results of photodegradation of MB and RhB (Fig. 7B). The photooxidative capability of the active sample obtained at 160 °C for •OH formation was 15 times higher than that of the commercial P25 TiO_2. The linear correlations between the fluorescence intensity and irradiation time confirmed the good stability of Ti^{3+} self-doped TiO_2(A)/TiO_2(R) heterojunctions.

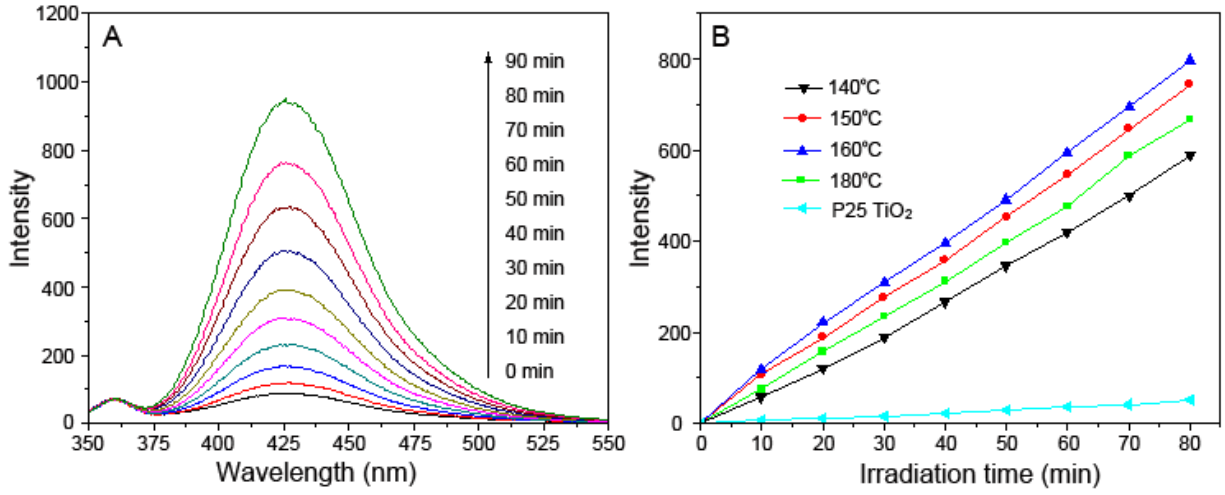

Fig. 7. (A) •OH trapping in the PL spectra during irradiation by using the heterojunctions obtained at 160 °C for 24 h in a 5×10^{-4} M TA solution (excitation wavelength, 320 nm). (B) Temporal dependence of the fluorescence intensity at 425 nm of visible-light irradiated using the heterojunction samples and P25 TiO_2.

3.4 Proposed mechanism for the enhanced photocatalytic activity

It is reported that Ti^{3+} and Ov play an essential role in photocatalytic process over TiO_2 photocatalyst. Ti^{3+} doping extended the absorption of TiO_2 to the visible region and the Ov on the particles surface can adsorb oxygen molecules and used as electron capture agent and results in the reduction of an electro-hole pair recombination rate.[37]

There are two types of Ti^{3+}, on kind is surface Ti^{3+} and the other is lattice Ti^{3+}. Each kind of Ti^{3+} ions has a special role in photocatalytic mechanism. Previous reports that the surface Ti^{3+} will capture O_2 to form O_2•−, HO_2•, and •OH with subsequent reactions and supporting both reduction and oxidation process.[38] The lattice Ti^{3+} will form localized states under CB bottom of TiO_2, so it can be stimulated by visible light.[39] The enhanced photocatalytic activities of Ti^{3+} self-doped TiO_2(A)/TiO_2(R) heterojunctions compared with those of P25 TiO_2 were attributed to the following reasons: (i) Ti^{3+} doping extended the absorption of TiO_2 to the visible region; (ii) separation of electron−hole pairs at the interface by the heterojunctions between TiO_2(A) nanoparticles and TiO_2(R) nanorods; (iii) promotion of the photocatalytic activity by the hydroxyl groups at the particle surface.

We proposed the transfer mechanisms based on the results: (i) interfacial electron transfer from the CB of TiO_2(A) to the CB of TiO_2(R); (ii) rapid electron transfer from the CB of TiO_2(R) to the low-energy lattice trapping sites of A.[40] Deak et al. reported that the bulk CB edge of R was ~0.35 eV above that of A, whereas the valence band offset was ~0.55 eV. The staggered alignment of the bands indicated that the migrating holes and electrons accumulated in R and A, respectively.[41] The differences between the band edges of the two phases could appropriately facilitate the charge

transfer. The photoexcited electrons in R migrated to the CB of A, whereas the holes in A migrated to the valence band of R; these results implied that the electron–hole recombination was suppressed.[42] Fig. 8 shows the synergetic mechanism of the visible-light response and separation of electron−hole pairs at the interface of TiO_2(A)/TiO_2(R) heterojunction.

The presence of Ti^{3+} and O_V introduced continuous states between the valence band and CB of TiO_2 (Fig. 8). These states expanded the optical absorption of the heterojunction samples based on their optical absorption spectra (Fig. 5). Under visible-light irradiation, the electrons could be excited from the valence band of TiO_2(R) to Ti^{3+} and O_V states, then from Ti^{3+} or O_V states to the CB of TiO_2(R). The electron transfer from the CB of TiO_2(R) to the CB of TiO_2(A) and the hole transfer from the valence band of TiO_2(A) to the valence band of TiO_2(R); this transfer inhibited the recombination of electron–hole pairs and increased their lifetimes (Fig. 8(1)).[14] For high Ti^{3+} concentrations, the Ti^{3+} sites functioned as electron traps; the photogenerated charge carriers were easily recombined at these sites to reduce the photocatalytic abilities of excess Ti^{3+}. The absorption intensities in the visible-light region decreased for low Ti^{3+} concentrations, which limited the visible-light photocatalytic activity. We believed that the hydrothermal treatment temperature is primarily enhanced the visible-light photocatalytic oxidation.

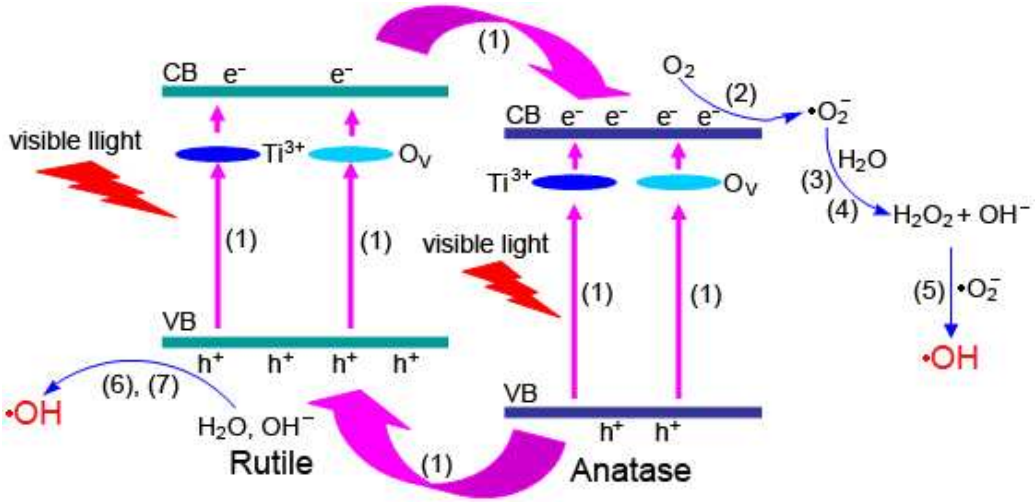

Fig. 8. Schematic of the charge migration and separation on Ti^{3+} self-doped TiO_2(A)/TiO_2(R) heterojunctions caused by visible-light irradiation and photocatalysis.

Under visible-light irradiation, the excited-state electrons transferred to the TiO_2(A) nanoparticle surface to react with dissolved oxygen and generate superoxide anion radicals ($\bullet O_2^-$) (Fig. 8(2)). $\bullet O_2^-$ became a highly oxidative •OH through a series of oxidation reactions (Figs. 8(3) to 8(5)). The holes could simultaneously oxidize the surface OH^- groups on the TiO_2(R) particles to generate •OH (Figs. 8(6) to 8(7)). The valence band holes could directly oxidize the organic molecules. Highly active species (e.g., $\bullet O_2^-$, •OH, or holes) were mainly caused the degradation of organic pollutants.[43] The reactions could be expressed as follows:

$$TiO_{2-x} + h\upsilon \rightarrow h_{VB}^+ + e^-_{CB} \quad (1)$$

$$O_2 + e^-_{CB} \rightarrow \bullet O_2^- \quad (2)$$

$$\bullet O_2^- + H_2O \rightarrow OH^- + \bullet HO_2 \quad (3)$$

$$\bullet HO_2 + \bullet HO_2 \rightarrow H_2O_2 + O_2 \quad (4)$$

$$H_2O_2 + \bullet O_2^- \rightarrow \bullet OH + OH^- + O_2 \quad (5)$$

$$OH^- + h^+ \rightarrow \bullet OH \quad (6)$$

$H_2O + h^+ \rightarrow \bullet OH + H^+$ (7)

The content of hydroxyl groups on the surface influenced the recombination rates of electron–hole pairs. The hydroxyl groups at the particle surface reacted with the holes in the valence band of TiO_2(R) and converted to highly reactive •OH radicals,[44] which were responsible for the photocatalytic activity. Hydrothermal treatments incorporated the hydroxyl groups at the particle surface and promoted the photocatalytic activity. The high crystallinity of TiO_2 was a requirement for high photocatalytic activity because the former reduced the amount of electron traps that functioned as recombination centers for electron–hole pairs.

The optimal photocatalytic activity of heterojunction samples obtained at 160 °C was attributed to the crystallinity and Ti^{3+} concentration. The samples obtained at 140 °C yielded the largest surface and the highest concentrations of Ti^{3+} and hydroxyl groups (Figs. 2A and 3B). However, the samples are mixtures of poorly crystallized and amorphous TiO_2; the content of TiO_2(R) was low (Fig. 1). Hence, the poor crystallinity and high Ti^{3+} concentration of the heterojunction samples increased the amount of electron traps that functioned as recombination centers; the photogenerated charge carriers were easily recombined at these sites. The low TiO_2(R) phase could not form an effective heterojunction, thereby decreasing its photocatalytic activity. The heterojunction exhibited the highest crystallinity and most abundant TiO_2(R) phase at 180 °C (Fig. 1), but obtained low concentrations of Ti^{3+} and hydroxyl groups (Figs. 3A and 3B). Moreover, low Ti^{3+} concentrations only produced localized O_V states that could deteriorate the electron mobility and yield a negligible visible-light photoactivity. The hydroxyl groups with low concentrations on the surface could not effectively trap holes to form oxidative •OH for the photodegradation of organic molecules. Hence,

the photocatalytic activity could not continuously increase with the treatment temperature. TiO_2(A)/TiO_2(R) heterojunction samples obtained at 150 °C and 160 °C yielded suitable amounts of Ti^{3+} and hydroxyl groups (Fig. 3) and exhibited a maximum absorption in the visible region (Fig. 5) Simultaneously, the samples obtained at 150 °C yielded smaller amounts of TiO_2(R) nanorods than those obtained at 160 °C (Figs. 1 and 2), thereby enhancing the heterojunctions and the photogenerated electron–hole separation and migration. This result allowed the electrons and holes to participate in the efficient photodegradation of MB and RhB.

4. Conclusions

In summary, Ti^{3+} self-doped TiO_2(A)/TiO_2(R) heterojunctions were synthesized by a simple and surfactant-free hydrothermal method at different hydrothermal treatment temperatures. The architecture of TiO_2(A)/TiO_2(R) heterojunctions and Ti^{3+} concentration could be controlled by adjusting the treatment temperature. The heterojunctions exhibited a redshifted absorption and better photocatalytic activity compared with those of commercial P25 TiO_2 in the photodegradation of MB and RhB under visible-light irradiation ($\lambda \geq 400$ nm). Ti^{3+} self-doping increased the light response range. The heterojunctions at the interface between TiO_2(A) nanoparticles and TiO_2(R) nanorods efficiently reduced the recombination of photoinduced electron–hole pairs and increased the lifetime of charge carriers 15 times that of P25 TiO_2.

Acknowledgments

This work was supported by the Key Project of Natural Science Foundation of Shandong Province

(ZR2013EMZ001), the National Basic Research Program of China (Grant No. 2013CB632401), and the Project of Shandong Province Higher Educational Science and Technology Program (J12LA01, J11LB03). This research has also been partially supported by the Program for Scientific Research Innovation Team in Colleges and Universities of Shandong Province.

References

[1] A. Kudo, Y. Miseki, *Chem. Soc. Rev.*, 2009, **38**, 253-278.

[2] L. M. Shen, N. Z. Bao, Y. Q. Zheng, A. Gupta, T. C. An, K. Yanagisawa, *J. Phys. Chem. C*, 2008, **112**, 8809-8818.

[3] P. Xu, T. Xu, J. Lu, S. M. Gao, N. S. Hosmane, B. B. Huang, Y. Dai, Y. B. Wang, *Energy & Environ. Sci.*, 2010, **3**, 1128-1134.

[4] C. H. Chen, Q. W. Liu, S. M. Gao, K. Li, H. Xu,, Z. Z. Lou, B. B. Huang, Y. Dai, *RSC Adv.*, 2014, **4**, 12098-12104.

[5] T. R. Gordon, M. Cargnello, T. Paik, F. Mangolini, R. T. Weber, P. Fornasiero, C. B. Murray, *J. Am. Chem. Soc.*, 2012, **134**, 6751-6761.

[6] X. Liu, H. Xu, R. G. Lauren, S. M. Gao, Z. Z. Lou, W. J. Wang, B. B. Huang , Y. Dai, T. Xu, *Catal. Today*, 2014, **225**, 80-89.

[7] Q. Zhu, Y. Peng, L. Lin, C. M. Fan, G. Q. Gao, R. X. Wang, A. W. Xu, *J. Mater. Chem. A*, 2014, **2**, 4429-4437.

[8] X. Liu, L. R. Grabstanowicz, S. M. Gao, H. Xu, Z. Z. Lou, W. J. Wang, B. B. Huang, Y. Dai, T. Xu, *Nanoscale*, 2013, **5**, 1870-1875.

[9] R. Sasikala, V. Sudarsan, C. Sudakar, R. Naik, L. Panicker, S. R. Bharadwaj, *Int. J. Hydrogen Energy*, 2009, **34**, 6105-6113.

[10] I. Justicia, P. Ordejón, G. Canto, J. L. Mozos, J. Fraxedas, G. A. Battiston, R. GeRhBasi, A. Figueras, *Adv. Mater.*, 2002, **14**, 1399-1402.

[11] T. A. Arun, D. K. Chacko, A. A. Madhavan, T. G. Deepak, G. S. Anjusree, T. Sara, S. Ramakrishna, S. V. Nair, A. S. Nair, *RSC Adv.*, 2014, **4**, 1421-1424.

[12] X. J. Lv, H. Zhang, H. X. Chang, *Mater. Chem. Phys.*, 2012, **136**, 789-795.

[13] J. Zhang, Q. Xu, Z. C. Feng, M. J. Li, C. Li, *Angew. Chem.*, 2008, **120**, 1790-1793.

[14] M. Addamo, M. Bellardita, A. D. Paola, L. Palmisano, *Chem. Commun.*, 2006, **47**, 4943-4945.

[15] Z. Y. Liu, X. T. Zhang, S. Nishimoto, M. Jin, D. A. Tryk, T. Murakami, A. Fujishima, *Langmuir*, 2007, **23**, 10916-10919.

[16] J. G. Li, T. Ishigaki, X. D. Sun, *J. Phys. Chem. C*, 2007, **111**, 4969-4976.

[17] H. Roussel, V. Briois, E. Elkaim, A. Roy, J. P. Besse, *J. Phys. Chem. B*, 2000, **104**, 5915-5923.

[18] R. A. Spurr, H. Myers, *Anal. Chem.*, 1957, **29**, 760-762.

[19] X. M. Song, J. M. Wu, M. Z. Tang, B. Qi, M. Yan, *J. Phys. Chem. C*, 2008, **112**, 19484-19492.

[20] M. N. Tahir, P. Theato, P. Oberle, G. Melnyk, S. Faiss, U. Kolb, A. Janshoff, M. Stepputat, W. Tremel, *Langmuir*, 2006, **22**, 5209-5212.

[21] N. C. Saha, H. G. Tompkins, *J. Appl. Phys.*, 1992, **72**, 3072-3079.

[22] J. Su, X. X. Zou, Y. C. Zou, G. D. Li, P. P. Wang, J. S. Chen, *Inorg. Chem.*, 2013, **52**, 5924-5930.

[23] S. H. Szczepankiewicz, J. A. Moss, M. R. Hoffmann, *J. Phys. Chem. B*, 2002, **106**, 2922-2927.

[24] Z. L. Xu, J. Shang, C M.. Liu, C. L. Kang, H. C. Guo, Y. G. Du, *Mater. Sci. Eng. B*, 1999, **63**, 211-214.

[25] J. Zou, J. C. Gao, Y. Wang, *J. Photochem. Photobio. A: Chem.*, 2009, **202**, 128-135.

[26] G. Liu, X. X. Yan, Z. G. Chen, X. W. Wang, L. Z. Wang, G. Q. Lu, H. M. Cheng, *J. Mater. Chem.*, 2009, **19**, 6590-6596.

[27] G. Krylova, A. Brioude, S. Ababou-Girard, J. Mrazeka, L. Spanhel, *Phys. Chem. Chem. Phys.*, 2010, **12**, 15101-15110.

[28] Y. Zhao, C. Z. Li, X. H. Li, F. Gu, H. L. Du, L. Y. Shi, *Appl. Catal. B: Environ.*, 2008, **79**, 208-215.

[29] Z. K. Zheng, B. B. Huang, X. D. Meng, J. P. Wang, S. Y. Wang, Z. Z. Lou, Z. Y. Wang, X. Y. Qin, X. Y. Zhang, Y. Dai, *Chem. Commun.*, 2013, **49**, 868-870.

[30] Y. Zhang, L. Z. Wu, Q. H. Zeng, J. F. Zhi, *J. Phys. Chem. C*, 2008, **112**, 16457-16462.

[31] a) S. Li, G. Ye, G. Chen, *J. Phys. Chem. C.*, 2009, **113**, 4031-4037; b) K. Yanagisawa, J. Ovenstone, *J. Phys. Chem. B.*, 1999, **103**, 7781-7787.

[32] C. K. Xu, D. Gao, *J. Phys. Chem. C*, 2012, **116**, 7236-7241.

[33] W. X. Guo, C. Xu, X. Wang, S. H. Wang, C. F. Pan, C. J. Lin, Z. L. Wang, *J. Am. Chem. Soc.*, 2012, **134**, 4437-4441.

[34] S. M. Prokes, J. L. Gole, X. Chen, C. Burda, W. E. Carlos, *Adv. Funct. Mater.*, 2005, **15**, 161-167.

[35] D. M. Guldi, G. M. A. Rahman, V. Sgobba, N. A. Kotov, D. Bonifazi, M. Prato, *J. Am. Chem. Soc.*, 2006, **128**, 2315-2323.

[36] Y. Hu, X. H. Gao, L. Yu, Y. R. Wang, J. Q. Ning, S. J. Xu, X. W. Lou, *Angew. Chem.*, 2013, **125**, 5746-5749.

[37] (a) J. Jun, M. Dhayal, J. H. Shin, J. C. Kim, N. Getoff, *Radiation Phys. Chem.*, 2006, **75**, 583–589, (b) L. B. Xiong, J. L. Li, B. Yang, Y. Yu, *J. Nanomater.*, 2012, **2012**, doi:10.1155/2012/831524. (c) X. D. Jiang, Y. P. Zhang, J. Jiang, R. S. Rong, Y. C. Wang, Y. C. Wu, C. X. Pan, *J. Phys. Chem. C*, 2012, **116**, 22619-22624..

[38] A. E. Giannakas, M. Antonopoulou, Y. Deligiannakis, I. Konstantinou, *Appl. Catal. B: Environ.*, 2013, **140–141**, 636–645.

[39] C. D. Valentin, G. Pacchioni, A. Selloni, *J. Phys. Chem. C*, 2009, **113**, 20543-20552.

[40] T. Kawahara, Y. Konishi, H. Tada, N. Tohge, J. Nishii, S. Ito, *Angew. Chem. Int. Ed.*, 2002, **41**, 2811-2813.

[41] P. Deak, B. Aradi, T. Frauenheim, *J. Phys. Chem. C*, 2011, **115**, 3443-3446.

[42] J. T. Carneiro, T. J. Savenije, J. A. Moulijn, G. Mul, *J. Phys. Chem. C*, 2011, **115**, 2211-2217.

[43] S. Murphy, C. Saurel, A. Morrissey, J. Tobin, M. Oelgemöler, K. Nolan, *Appl. Catal. B: Environ.*, 2012, **119**, 156-165.

[44] M. Vijay, P.V. Ananthapadmanabhan, K.P. Sreekumar, *Appl. Surf. Sci.*, 2009, **255**, 9316-9322.